aerospace

MDPI

Article

Unsteady Numerical Investigation on the Sealing Effectiveness and Flow Field in Different Rim Seal Geometries

Qingcai Zhang [1], Qinqin Wang [2,3], Xiaoming Tan [1,*] and Jingzhou Zhang [1]

[1] College of Energy and Power Engineering, Nanjing University of Aeronautics and Astronautics, Nanjing 210016, China
[2] AECC Sichuan Gas Turbine Establishment, Chengdu 610500, China
[3] School of Energy and Power Engineering, Beihang University, Beijing 100191, China
* Correspondence: txmyy@nuaa.edu.cn

Abstract: A rim seal is often used to prevent the ingress of high-temperature gas into the turbine disk cavity and protect the turbine disk from damage. Based on the overlapping rim seal (Seal-A), this paper proposes two more composite sealing structures (Seal-B and Seal-C) to show the effects of a deep cavity in the static disk and a modified platform in the rotating disk. Three-dimensional unsteady Reynolds-averaged Navier–Stokes equations and the shear stress transfer (SST) k-ω turbulence model were used to reveal the flow field characteristics and the sealing efficiency. The results show that the rotor–stator interaction plays a dominant role in the sealing outlet pressure, and the sealing efficiency in the outflow area obtained by the transient calculation is lower than that of the steady-state calculation. The rise in the cooling air flow enhances the reverse vortex in the sealing cavity, and the disk cavity's sealing efficiency is also improved. When the cooling air flow ratio increases from 0.6% to 1.8%, the sealing efficiency at the high radius increases by 30%. The shape of the deep cavity produces a new return vortex at the lower part of the sealing cavity, which improves the sealing efficiency. The shark nose platform in Seal-C aggravates the gas ingress at the sealing outlet but improves the sealing efficiency at the sealing cavity. In general, compared with Seal-A, the sealing efficiency of Seal-B and Seal-C is increased by 13.5% and 10%, respectively, at a cooling air flow ratio of 0.6%.

Keywords: turbine; overlapping rim seal; unsteady flow; gas ingress; sealing efficiency

check for updates

Citation: Zhang, Q.; Wang, Q.; Tan, X.; Zhang, J. Unsteady Numerical Investigation on the Sealing Effectiveness and Flow Field in Different Rim Seal Geometries. *Aerospace* **2022**, *9*, 780. https://doi.org/10.3390/aerospace9120780

Academic Editor: Jian Liu

Received: 3 October 2022
Accepted: 29 November 2022
Published: 1 December 2022

1. Introduction

The clearance between the rotating and the static disks in an aero-engine high-pressure turbine can easily cause gas ingress, resulting in ablation damage to the internal components of the disk cavity [1–3]. A sealing structure is often used in the turbine disk cavity, and cooling air is introduced from the compressor to increase the pressure in the disk cavity to prevent gas ingress [4–6]. On the one hand, excessive cooling air can cause energy loss, such as mainstream pressure and heat energy, reducing turbine efficiency. On the other hand, too little cooling air cannot resist the ingress of high-temperature gas. Therefore, the design of the sealing structure is crucial. Using an efficient sealing structure can ensure better sealing in the disk cavity and significantly reduce the required cooling air, which is of great significance to the turbine performance and overall engine design [7–10].

Numerous numerical and experimental studies have been carried out to investigate the gas ingress characteristics of the rim seal. Phadke and Owen [11–14] conducted a series of experimental studies to understand the variation of the sealing efficiency and minimum sealing flow rate with rotational speed. Owen [15,16] continued to conduct theoretical and numerical studies of the gas ingress mechanisms and classified the gas ingress as externally induced or rotationally induced. According to the orifice plate model and experimental data, the predicted minimum sealing flow rate for each ingress mechanism is also given, laying the foundation for subsequent research on rim seals.

Sangan [17–19] used the tracer gas measurement method to investigate the gas ingress characteristics of different sealing structures in a single turbine stage test stand and also studied the effect of mainstream flow rate, rotational speed, and cooling air flow on the gas ingress characteristics of various sealing structures. The studied sealing structures included axial rim seals, radial rim seals, and double rim seals. The research results show that the gas ingress of the radial seal is less than the axial seal under the same working conditions, and the double seal structure can better resist gas ingress into the inner cavity. Sangan [20] continued to study and found a method of adding fins to the sealing structure based on the above experimental studies. The results showed that the sealing cavity pressure increases after adding fins, which helps reduce the ingress of mainstream high-pressure gas to improve the sealing performance.

Jia et al. [21] conducted numerical simulations on the radial–axial rim seal using actual working parameters and found that the sealing efficiency of a radial–axial rim seal was higher than for a simple rim seal. Savov [22] studied the single-lip and double-lip sealing structures and found that the sealing performance of the double-lip rim seal was significantly better than the single-lip rim seal. When the same sealing effect was achieved, the cooling airflow required for a double-lip rim seal was less than that for a single-lip rim seal.

Popovic and Hoson [23] conducted a series of experimental and numerical investigations on the overlapping rim seal and its improved rim seal. The results showed that the overlapping rim seal has a high sealing efficiency, and the outer cavity of the overlapping rim seal can retain a large amount of high-temperature gas, increasing the inner cavity sealing efficiency. Moon [24] conducted a detailed study on the position and geometric parameters of the sealing teeth on the overlap based on the overlapping rim seal. It was found that installing overlapping teeth can prevent the ingress of mainstream gas and improve the overlapping rim seal's performance. The height of the sealing teeth significantly impacts the sealing characteristics, while their width has little influence, and there is an optimal installation position. Soghe et al. [25] proposed a sealing structure with a deep cavity in the static disk and compared the effect of cavity geometric parameters on the sealing efficiency. Scobie et al. [26] proposed a complex "Angelwing" sealing structure in which the disk cavity flow path is designed as a complex cavity that can prevent gas ingress by increasing gas resistance. Experimental and numerical research showed that the "Angelwing" sealing structure could achieve high sealing efficiency at low sealing flow rates.

Popovic [24] and Schuler [27,28] not only studied the cavity structure of the overlapping rim seal but also designed the platform's structure. The results showed that using the improved platform could reduce the temperature in the leaf root region of the blade and the aerodynamic loss but did not improve the sealing performance of the overlapping rim seal. Li et al. [29] conducted an unsteady numerical study on a radial sealing structure with a honeycomb surface. The results showed that the honeycomb surface arranged on the inner tooth surface of the radial rim seal could improve the sealing performance to a greater extent than the traditional radial rim seal, and the sealing efficiency can be increased by 9–14%. In addition, the depth of the honeycomb hole has an important influence on the sealing performance, with a deeper honeycomb hole corresponding to a higher sealing efficiency.

Erickson [30] proposed two bionic ("dolphin nose" and "shark nose") platform structures and focused on their gas ingress characteristics. The results showed that the gas ingress of the dolphin nose sealing structure was lower than the shark nose sealing structure. Zhang et al. [31] conducted experimental and numerical studies on the rim seal with the dolphin nose platform and rim seals with different cavities based on the shark nose sealing structure. Their research showed that the structure of the dolphin nose platform and its hook shape caused a cooling air rotary vortex in the sealing cavity, allowing the dolphin nose platform rim seal to achieve high sealing efficiency.

In summary, many researchers have studied rim seal gas ingress characteristics and structural design. Among them, there is little research on the sealing characteristics of the rim seals with a deep cavity in the static disk or a modified platform in the rotating disk, and there is also a lack of relevant unsteady numerical investigations. Therefore, this paper proposes two composite sealing structures (Seal-B and Seal-C) based on the overlapping rim seal (Seal-A). Seal-B only has a deep cavity in the static disk, and Seal-C contains a deep cavity in the static disk and the shark nose platform in the rotating disk. The flow at the sealing clearance is highly unsteady, and the steady numerical method cannot obtain the gas ingress characteristics under the influence of rotor–stator interaction [32–34]. For this reason, it is necessary to carry out an unsteady numerical study of the rim seal. In this paper, the unsteady flow characteristics at the sealing clearance are analyzed, and the influence of cooling air flow rates and sealing structures on the flow field and sealing characteristics is revealed, providing a reference for the design and optimization of sealing structures.

2. Computational Model and Numerical Method

2.1. Computational Model

The model studied in this paper is obtained by simplifying the first high-pressure turbine stage of a current aero-engine application. As shown in Figure 1, the turbine stage has 30 vanes and 60 blades, which are periodic in the circumferential direction. One vane passage, two blade passages, and a 12-degree disk cavity sector are chosen as the computational domain. The sealing structure in the calculation model is Seal-A, used as the baseline seal configuration in this paper. The fluid domain where the vane is located is the stationary domain, and the fluid domain where the blade is located is the rotating domain. The rotating–stationary domain interface is set upstream of the rim seal. The height of the main flow channel is approximately 60 mm. The length of the inlet development section is more than 1.5 times the axial chord length of the vane, and the distance between the outlet and the blade trailing edge is more than 1.5 times the axial chord length of the blade. The blade tip clearance influence on the turbine flow is not considered.

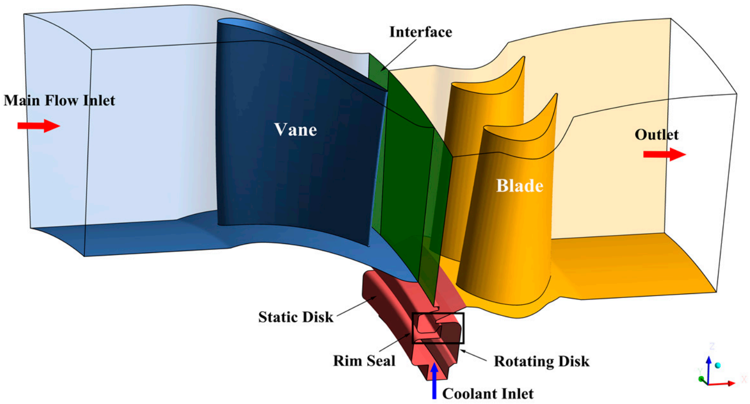

Figure 1. Computational domain of turbine rim seal.

The subject of this research is the sealing structure between the stationary disk and the rotating disk. Figure 2 shows the geometric configurations of three sealing structures. Seal-A, the baseline seal structure used in this study, is based on the overlapping rim seal with a hook on the lower surface of the sealing cavity. Seal-B uses a deep cavity in the static disk to the sealing cavity based on Seal-A. Seal-C further modifies the upper surface of the platform to a concave surface. The change in sealing structure only occurs in the sealing cavity, and the inner cavity structure remains unchanged. For Seal-A, the outer radius of the disk cavity is b = 287 mm, and the distance between the stationary disk and the rotating disk is $S = 0.06b$. The axial clearance of the rim seal is $S_{ax} = 0.02b$, and the radial clearance is $S_{rad} = 0.003b$. The radial clearance of the three sealing structures is consistent. The main purpose of Seal-B is to investigate the effect of the deep cavity structure on the flow field and sealing performance. The main purpose of Seal-C is to further investigate the modified platform's effect on the flow field and sealing efficiency.

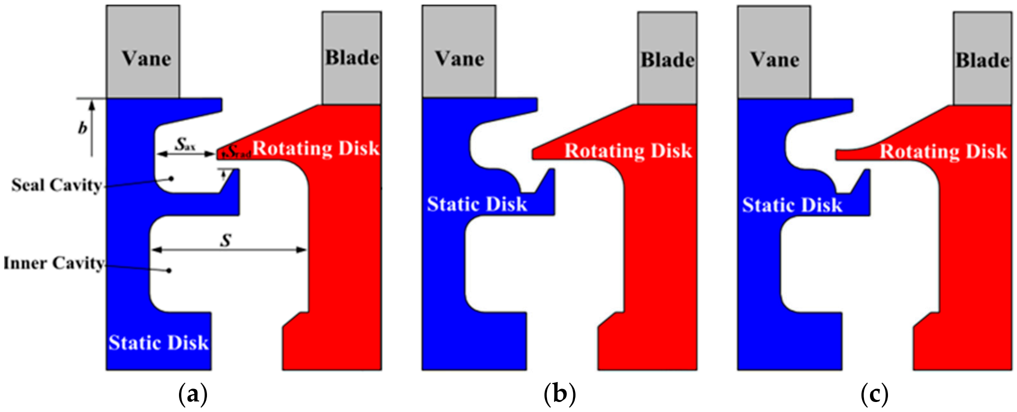

(**a**) (**b**) (**c**)

Figure 2. Meridional structural configuration of the turbine rim seals. (**a**) Seal-A; (**b**) Seal-B; and (**c**) Seal-C.

2.2. Data Reduction

The rotational Reynolds number is defined as

$$Re_{\Omega} = \frac{\rho \omega b^2}{\mu} \tag{1}$$

where ρ and μ are the density and dynamic viscosity of the airflow, respectively, and ω is the rotational angular velocity.

The axial Reynolds number in the annulus is defined as follows [35]

$$Re_w = \frac{\rho v b}{\mu} \tag{2}$$

where v is annulus axial velocity.

The dimensionless angle is defined as

$$\theta^* = \frac{\theta - \theta_0}{\theta_1 - \theta_0} \tag{3}$$

where θ_0 and θ_1 are the minimum and maximum circumferential angles, respectively, of the axial position where the measuring point is located, and θ is the circumferential angle of the measuring point.

The pressure coefficient is defined as

$$C_p = \frac{p_s}{p_{t,in}} \tag{4}$$

where P_s is the static pressure, and $P_{t,in}$ is the total pressure at the mainstream annulus inlet.

The sealing efficiency is defined as

$$\varepsilon = \frac{c - c_\infty}{c_{coolant} - c_\infty} \tag{5}$$

where c is the CO_2 concentration at the measuring point, $c_{coolant}$ is the CO_2 concentration at the cooling air inlet, and c_∞ denotes the CO_2 concentration at the annulus inlet.

2.3. Calculation Method

Because of the rotational characteristics of this model, the unsteady gas ingress and sealing efficiency of three kinds of rim seals are investigated by numerically solving the three-dimensional unsteady Reynolds-averaged Navier–Stokes (URANS) equations and SST k-ω turbulence model [36] using the ANSYS CFX 14.5 commercial software. The time step is 1.7857×10^{-6} s, corresponding to 80 physical time steps for one blade passing. Ten iterations are required in a single physical time step. The converged results of a stationary calculation are selected as the initial conditions for the unsteady calculation. The standard for computational convergence is for the residuals to be below 10^{-5}, for the monitoring point parameters to show periodic variations with time, and to be maintained for more than two rotation periods. The convergence curves of the main flow pressure and sealing efficiency in the disk cavity with time step at the flow ratio IF = 0.6% (where IF is the ratio of the cooling airflow rate to the mainstream flow rate) are given in Figure 3. The calculation converges after approximately 5000 time steps, and 800 time steps are required to obtain the unsteady time-averaged results.

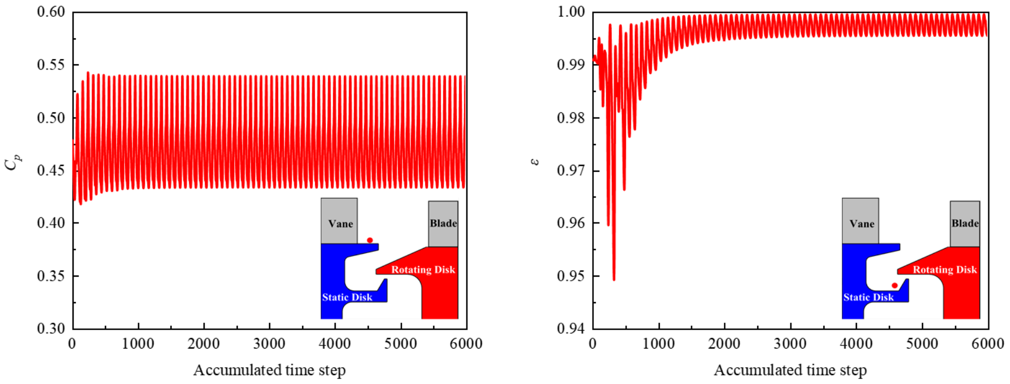

(**a**) (**b**)

Figure 3. Unsteady pressure and sealing effectiveness convergence history curves. (**a**) downstream of the vane trailing edge; and (**b**) sealing cavity.

The tracer variable method is used in the numerical calculations, the additional tracer variable and the additional variable turbulent transport equation are adopted to predict the transport and diffusion process of the tracer gas (CO_2) in the mainstream passage and the disk cavity [37–39]. The equation in scalar form is:

$$\frac{\partial(\rho\varphi)}{\partial t} + \nabla\cdot(\rho U\varphi) = \nabla\left(\left(\rho D_\phi + \frac{\mu_t}{Sc_t}\right)\nabla\varphi\right) \tag{6}$$

The above equation describes the diffusion and turbulent transport processes of the computational domain units, where U is the fluid velocity, ρ is the mixture density, φ is the conserved quantity per unit volume or concentration, $\varphi = \varphi/\rho$ is the conserved quantity per unit mass, D_φ is the kinematic diffusivity for the scalar, Sc_t is the turbulent Schmidt number, and μ_t is the turbulent viscosity.

The additional variable of the coolant inlet is set to 1, and that of the annulus inlet is set to 0. When the mainstream gas and sealing cooling air are mixed, the value of the additional tracer variable is between 0 and 1. According to Equation (5), the sealing efficiency is the same as the additional variable value.

2.4. Grid Independence Study

The turbine stage model with the sealing structure studied in this paper is complex. The profile curvature of the blade is large. Therefore, the model uses an unstructured mesh generated using ICEM CFD. A boundary layer grid is used around the main flow channel, vane, blade, and other wall surfaces. Figure 4 shows the mesh details near the blade and inside the cavity. The first layer of the grid is located 1 μm from the wall surface, and the maximum y^+ value is less than 1, which meets the requirements of the SST k-ω turbulence model.

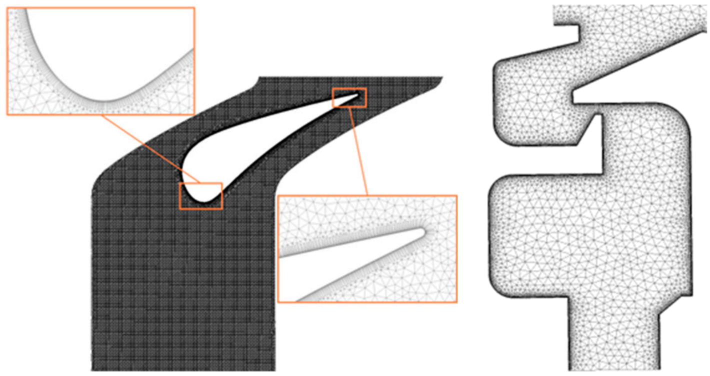

(**a**) (**b**)

Figure 4. Computational mesh in the fluid domain: (**a**) main flow passage; and (**b**) sealing cavity.

To minimize the error at the stationary–rotating domain interface, the circumferential and radial nodes of the interface are ensured to be consistent when creating the mesh. As shown in Figure 5, when the control volumes exceed 12 million, both the difference among circumferential pressure curves and the difference among circumferential temperature curves at the sealing outlet are below 5%, meeting the grid independence verification condition. A grid with approximately 14 million control volumes is selected for the final numerical simulations.

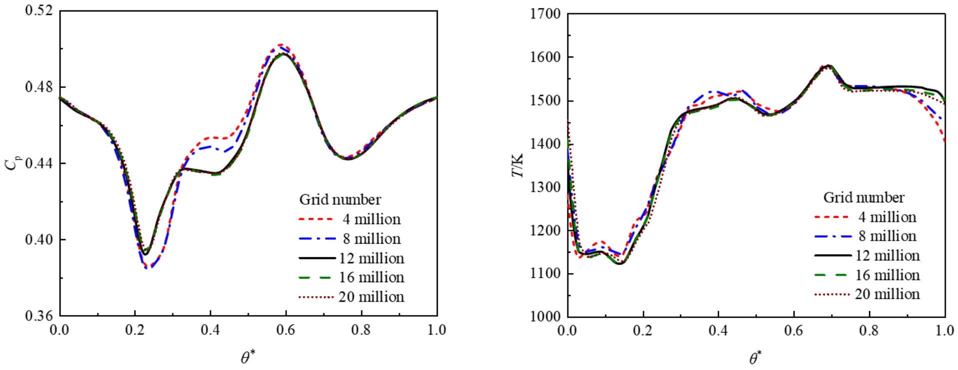

(**a**) (**b**)

Figure 5. Grid independence test results: (**a**) the circumferential static pressure distribution at the sealing exit; (**b**) the circumferential temperature distribution at the sealing exit.

2.5. Boundary Conditions

The working conditions studied in this paper are close to actual engine operating conditions. Table 1 details the boundary conditions used in the calculations. The mainstream inlet condition and the coolant inlet condition are specified as mass flow rates, and the axial Reynolds number in the annulus is 2.15×10^6. The total temperature of the mainstream inlet is 1760 K, and the temperature at the coolant inlet is 800 K. The outlet condition of the single turbine stage is a mean static pressure of 629,500 Pa. The rotational Reynolds number is 1.27×10^7. Five ratios of the cooling air flow rate to mainstream flow rate (*IF*) of 0%, 0.6%, 1.2%, 1.8%, and 2.4% are used.

The working fluid is modeled as an ideal gas. The wall conditions for the blade, hub, and rim seal are set as smooth, adiabatic, and no-slip walls. Rotationally periodic interfaces are specified for the circumferential surfaces of the mainstream channel and the disk cavity. The domain interface is set to a transient rotor–stator condition. High resolution is used for the numerical calculation difference format.

Table 1. Boundary conditions.

Boundary Condition	Value
Axial Reynolds number in annulus, Re_w	2.15×10^6
Rotational Reynolds number, Re_φ	1.27×10^7
Ratios of the cooling airflow rate to the mainstream flow rate (IF)/%	0%, 0.6%, 1.2%, 1.8%, 2.4%
Inlet total temperature in annulus/K	1760
Inlet static temperature in cooling airflow/K	800
Outlet static pressure/Pa	629,500

2.6. Validation of Numerical Method

Figure 6 gives the schematic diagram of the experimental system. A turbine rim seal experiment was carried out to verify the accuracy of the numerical simulation method. From Figure 6a, it can be seen that the centrifugal fan provides the steady airflow required by the mainstream of the test section. The airflow provided by the compressor passes through the filter and enters the stabilizing box. After mixing and stabilizing with the carbon dioxide gas, the required sealing air is formed. Figure 6b shows the cross-section of the test section with Seal-A. The outer radius of the disk cavity (b_{EXP}) is 220 mm, and the mainstream channel height (H) is 0.045 b_{EXP}. The remaining structural parameters of the sealing cavity are consistent with those in numerical model.

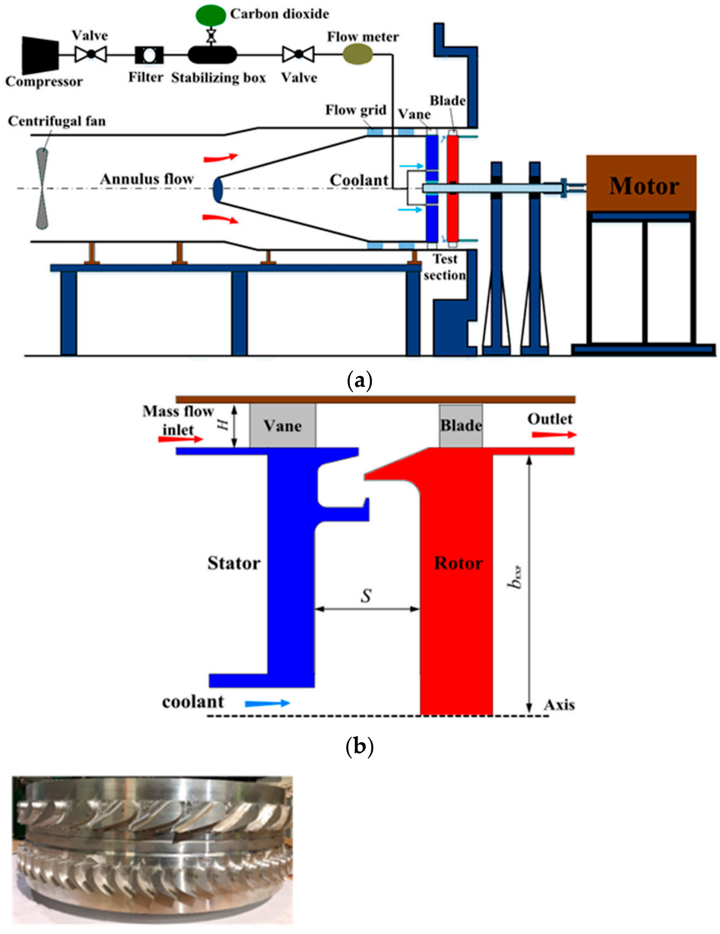

(a)

(b)

(c)

Figure 6. Experimental system in the present study: (**a**) experimental system; (**b**) test section; (**c**) and experimental rig.

The sealing cooling air flow (0.002 kg/s), the rotating Reynolds number (4.8×10^5), and three main flow ratios (*IR* = 0.4%, 0.6%, 1.2%) are selected to conduct experiments. Figure 7 gives the comparison between numerical simulation results and experimental results. Figure 7a shows the circumferential pressure distributions at the trailing edge of the vane. Figure 7b shows the sealing efficiency distributions along the disk cavity radial direction. It can be seen from the figure that the various laws of the pressure curve and the sealing efficiency curve obtained from the experiment are consistent with those obtained from the numerical simulation. The maximum relative errors of the static pressure coefficient and the sealing efficiency are 1% and 4.62%, respectively. Therefore, from the comparison of results, it can be considered that the error is within the acceptable range. The numerical method used in this paper can accurately simulate the flow characteristics of turbine rim seals.

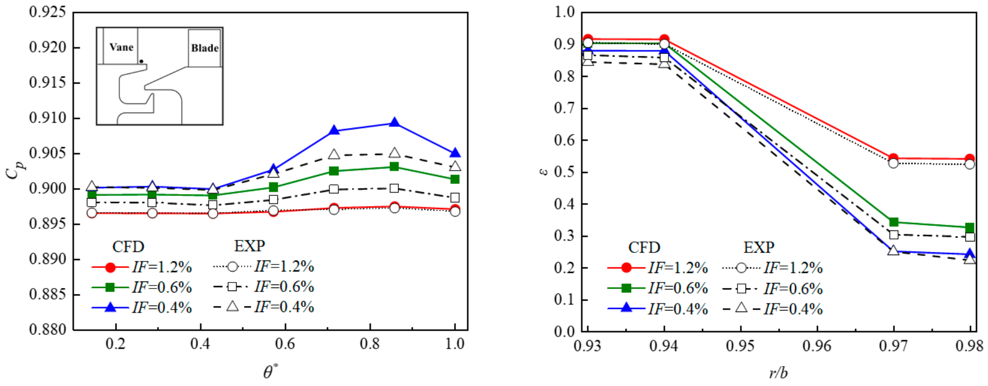

(**a**) (**b**)

Figure 7. Comparison of the results of numerical simulation and experimental results. (**a**) Circumferential pressure distribution downstream of the vane. (**b**) Sealing efficiency distribution along the disk cavity radial direction.

3. Results and Discussion

In this paper, the unsteady numerical calculation method is used to study the sealing characteristics of the rim seal. First, the unsteady characteristics of the sealing clearance are analyzed, and the relevant dependencies are obtained. Then, the influence of the cooling air flow rate on the flow characteristics and sealing performance is studied. Finally, the flow field and sealing characteristics of Seal-A, Seal-B, and Seal-C for typical working conditions are compared and analyzed. The effects of deep cavity in the stationary disk and the modified platform on the sealing performance are obtained.

3.1. Analysis of Unsteady Characteristics

A monitoring point was selected at the sealing outlet of Seal-A to reveal the flow characteristics under a high load operating environment, and the pressure was sampled at each time step during the unsteady numerical calculations.

Figure 8 shows the frequency characteristics of the monitoring pressure at the sealing outlet obtained by a fast Fourier transform, where the horizontal coordinate is the dimensionless frequency, and f_{blade} is the frequency at which the blade rotates through the vane channel. It can be seen from Figure 8 that the sealing clearance exit pressure is affected by many conditions, among which the interference between the blade and vane has a significant effect, corresponding to $f/f_{\text{blade}} = 1$ in the figure. A similar conclusion was obtained by Wang [40] in an unsteady numerical study of the model with a 1:2 vane-to-blade ratio under experimental operating conditions. The main influencing frequency is f_{blade}. When the leading edge of the blade meets the high-pressure area of the vane trailing edge, the maximum pressure occurs at the sealing exit, and the ingress is the largest.

The relative positions of the vane and blade at different instants are shown in Figure 9. The time for the blade to pass through a vane channel is *T*, and the time between two adjacent instants in Figure 9 is $1/4T$. The circumferential pressure distribution at the sealing outlet is shown in Figure 10. The pressure curve shows that at $(74 + 1/2)T$ and $(74 + 1)T$, the trailing edge of the vane meets the leading edge of one of the two blades. The high-pressure area at the trailing edge of the vane and the high-pressure area at the blade's leading edge are coupled with each other. The pressure reaches its maximum value at the trailing edge of the vane and is much higher than the time-averaged value. This is consistent with the behavior in the pressure spectrum analysis in Figure 8.

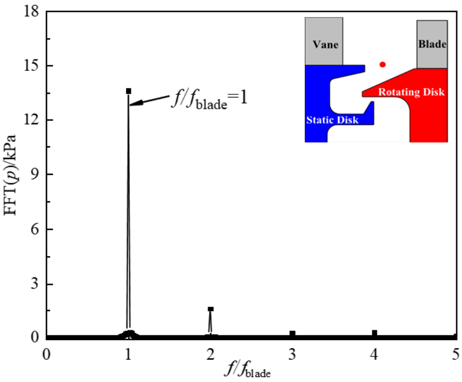

Figure 8. Pressure–frequency curve for the monitoring point at the clearance outlet (Seal-A and $IF = 0.6\%$).

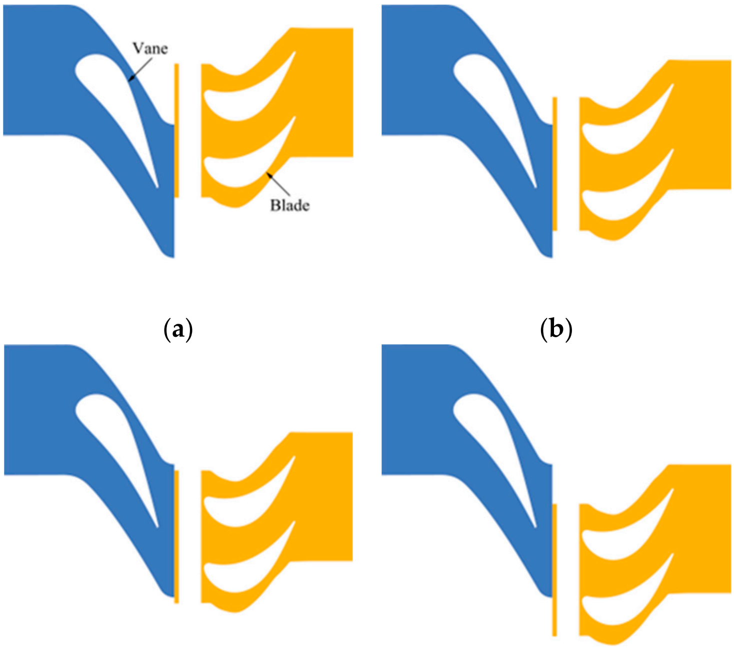

(**a**) (**b**)

(**c**) (**d**)

Figure 9. Relative locations of the blades and vane at different times: (**a**) $(74 + 1/4)T$; (**b**) $(74 + 1/2)T$; (**c**) $(74 + 3/4)T$; (**d**) $(74 + 1)T$.

At times $(74 + 1/4)T$ and $(74 + 3/4)T$, the blade's leading edge is far from the trailing edge of the vane. The trailing flow of the vane flows into the blade channel, the interaction with the blade's leading edge is weakened, the maximum pressure is reduced, and the pressure fluctuation is reduced. The time-averaged pressure is calculated by averaging the pressure at each moment, smoothing the pressure fluctuation characteristics. However, the distribution characteristics of higher pressure at the blade leading edge ($\theta^* \approx 0.25$ and $\theta^* \approx 0.75$) and lower pressure at the blade channel's leading edge can still be found from the curve distribution.

In the steady-state calculation, the relative position of the vane and blade does not change. The trailing edge of the vane is adjacent to the blade's leading edge, and the pressure distribution trend is similar to (74 + 1)*T*. By comparing the transient and steady-state pressure circumferential distributions, it can be seen that the pressure peak is higher for the transient calculation than for the steady-state calculation, and the pressure valley for the transient calculation is lower than for the steady-state calculation. The circumferential pressure difference obtained from the transient calculation is much larger than the steady-state result. Therefore, the circumferential pressure fluctuation at the sealing outlet obtained from the steady-state calculation is smaller than from the transient calculation result, leading to more significant gas ingress in the transient calculation.

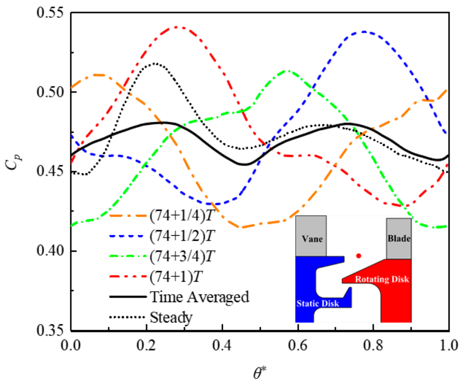

Figure 10. Transient and steady static pressure coefficient distribution along the circumferential direction at the clearance outlet (Seal-A and *IF* = 0.6%).

The change in the relative positions of the vane and blades affects the pressure distribution in the outlet area of the sealing clearance, which in turn affects the gas ingress and egress flow at the clearance. Figure 11 shows the pressure contours at the hub surface and the radial velocity contours at the sealing clearance exit at different times. The radial velocity directly reflects the gas ingress and egress flow at the sealing clearance. A radial velocity above zero indicates egress flow, and a radial velocity below zero indicates gas ingress.

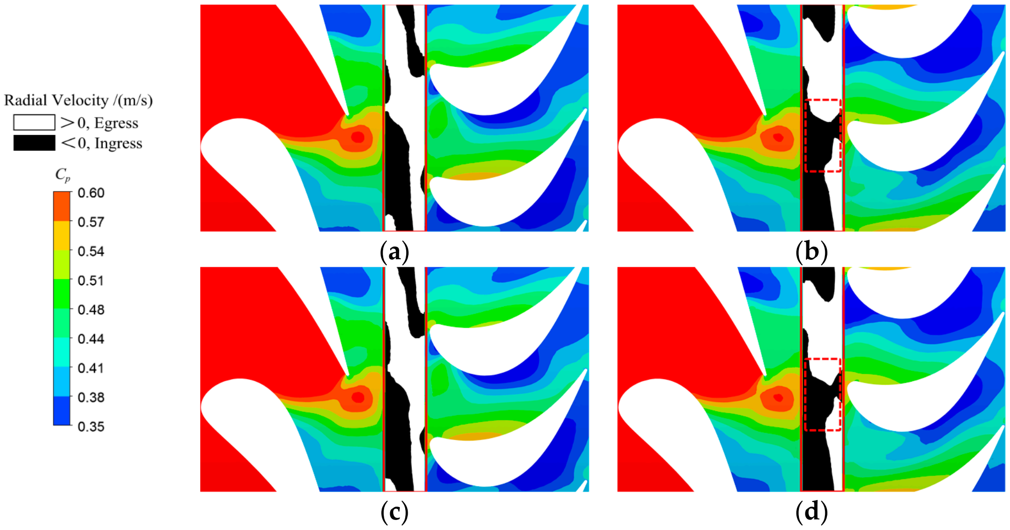

Figure 11. Radial velocity contour distributions at the clearance outlet and static pressure coefficient distributions at the endwall (Seal-A and *IF* = 0.6%). (**a**) (74 + 1/4)*T*; (**b**) (74 + 1/2)*T*; (**c**) (74 + 3/4)*T*; (**d**) (74 + 1)*T*.

As shown in the red dotted boxes in Figure 11 at (74 + 1/2)*T* and (74 + 1)*T*, the high-pressure area between the trailing edge of the vane and the leading edge of the blade results in a large negative radial velocity area at the clearance exit. The negative radial velocity area at the sealing clearance is relatively large, and more mainstream gas intrudes into the disk cavity. At (74 + 1/4)T and (74 + 3/4)T, the radial velocity at the sealing clearance is influenced by the vane trailing edge flow, and the negative radial velocity is mainly distributed in the region affected by the vane trailing edge flow. Compared with (74 + 1/2)T and (74 + 1)T, the negative radial velocity region area decreases, and the area of the positive radial velocity region increases at (74 + 1/4)T and (74 + 3/4)T. In other words, the gas ingress is relatively weaker, and the egress flow is relatively stronger.

The circumferential distribution of the sealing efficiency in the outflow area at the sealing outlet is given in Figure 12. The transient calculation results are time-averaged values. By comparing the sealing efficiency curves, it can be seen that the sealing efficiency at the sealing outlet obtained by the steady-state calculation is higher than for the transient calculation. This is because the vane–blade interaction, the unsteady flow characteristics of the vane trailing flow, and other flow characteristics are considered in the transient calculation. These causes increase the ingress of mainstream gas, thus reducing the sealing efficiency. Therefore, the sealing efficiency at the disk cavity under steady-state calculation is higher than that under the transient calculation.

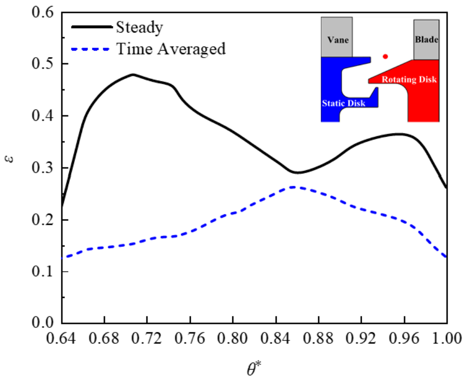

Figure 12. Circumferential distribution of sealing effectiveness at the sealing outlet (Seal-A and *IF* = 0.6%).

3.2. Influence Analysis of Cooling Air Flow Rate

According to the gas ingress mechanism, it is known that externally induced ingress is the main ingress pathway. The mainstream gas flows into the disk cavity when the local pressure in the mainstream channel is higher than in the disk cavity. Egress flow occurs when the pressure in the mainstream channel is less than in the disk cavity. The circumferential pressure distribution around the endwall is closely related to the ingress and egress flows.

Figure 13 shows the time-averaged static pressure coefficient C_p distribution in the circumferential direction at $l1$ (downstream of the vane trailing edge) and $l2$ (upstream of the blade leading edge). It can be seen from Figure 13a that the static pressure just downstream of the vane trailing edge at the five flow ratios shows the same fluctuation in the circumferential direction. The pressure peak at θ^* = 0.6 corresponds to high pressure at the vane trailing flow, which causes gas ingress into the disk cavity. The pressure peak at θ^* = 0.3 is due to the shock wave on the suction surface of the vane, with a high-pressure region appearing after the shock wave. Adding cooling air flow strengthens the egress flow, influencing the pressure field at the clearance outlet and in turn affecting the circumferential pressure distribution downstream of the vane trailing edge and upstream of the blade leading edge. Increasing the cooling air flow significantly improves the pressure coefficients at $l1$.

As seen in Figure 13b, the pressure peaks at θ^* = 0.2 and θ^* = 0.7 correspond to the high pressure at the two blade leading edges. The higher pressure in this region is due to the potential field at the leading edge of the blades. Adding cooling air flow increases the pressure coefficients at *l*2. The pressure peaks constantly approach the airflow stagnation point at the blade's leading edge, and the pressure valleys approach the middle region of the blade cascade channel. As the cooling air flow ratio increases from 0% to 2.4%, the C_p differences in the circumferential direction at *l*1 and *l*2 are reduced by 6.85% and 20.55%, respectively.

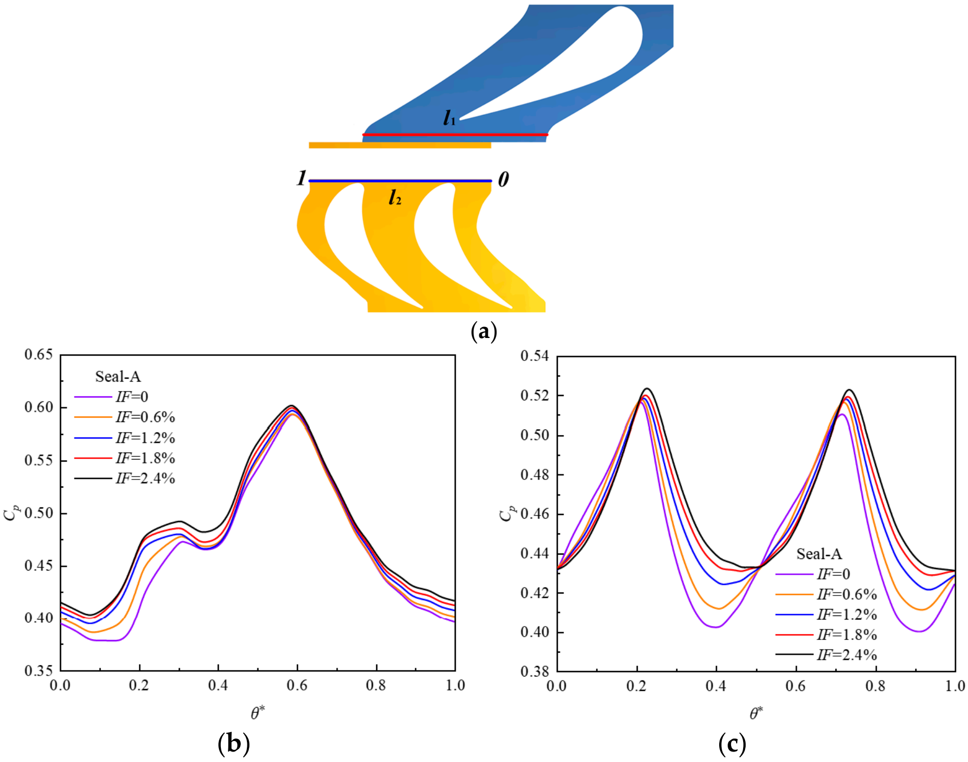

(**a**)

(**b**) (**c**)

Figure 13. Time-averaged static pressure coefficient C_p at the clearance outlet endwall along the circumferential curve: (**a**) position of curves on the vane endwall and the blade endwall; (**b**) vane endwall; (**c**) blade endwall.

Figure 14 presents the time-averaged C_p contour distributions at the endwall and the radial velocity contour distributions at the clearance outlet. From the radial velocity contour at the sealing clearance, the negative radial velocity region is mainly close to the high-pressure regions such as the vane trailing edge, the vane suction surface, and the blade leading edge. These areas correspond to the peak pressure areas in Figure 13, and the negative radial velocity areas are mainly located at the stationary disk side. The positive radial velocity region is far from these high-pressure regions, and the egress flow is mainly near the rotating disk side and in the front area of the rotor cascade passage, as shown in the red-dashed box in the figure.

Comparing the time-averaged C_p and radial velocity contours of Seal-A at the three flow ratios, the negative radial velocity region decreases continuously as the cooling air flow increases. This region is consistently concentrated in high-pressure areas, such as the vane trailing edge and blade leading edge, and the positive radial velocity region expands. In addition, the cooling airflow increases C_p, both downstream of the vane trailing edge and upstream of the blade leading edge, corresponding to the results in Figure 13.

To clarify the flow state in the sealing clearance, the time-averaged tangential and radial velocity distributions along the axial direction in the middle section of the sealing cavity (r/b = 0.98) are given in Figure 15. Here, x/S_{rad} = 0 is defined as the axial position of the stationary disk wall, and x/S_{rad} = 1 is defined as the axial position of the rotating disk wall. From Figure 15a, a consistent tangential velocity variation trend occurs in the middle section of the sealing cavity for the three flow ratios, and the tangential velocity increases as the axial position approaches the rotating disk. By comparing the tangential velocity curves for the three flow ratios in Figure 15a, it is found that an increasing flow ratio raises the tangential velocity values at each position in the axial direction.

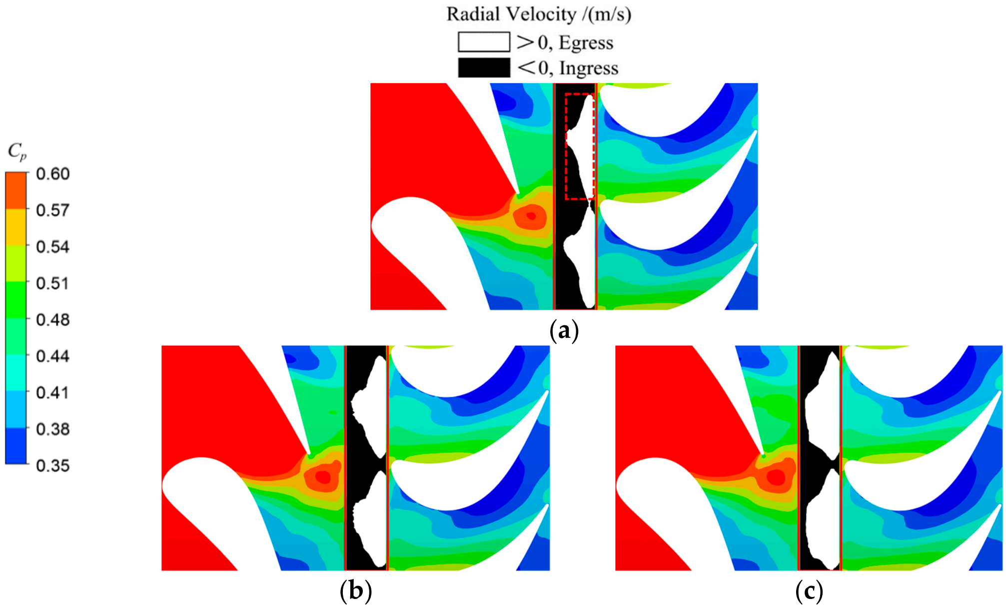

(**a**)

(**b**) (**c**)

Figure 14. Radial velocity contour distribution at the clearance outlet and static pressure coefficient distribution at the endwall. (**a**) *IF* = 0.6%; (**b**) *IF* = 1.2%; (**c**) *IF* = 1.8%.

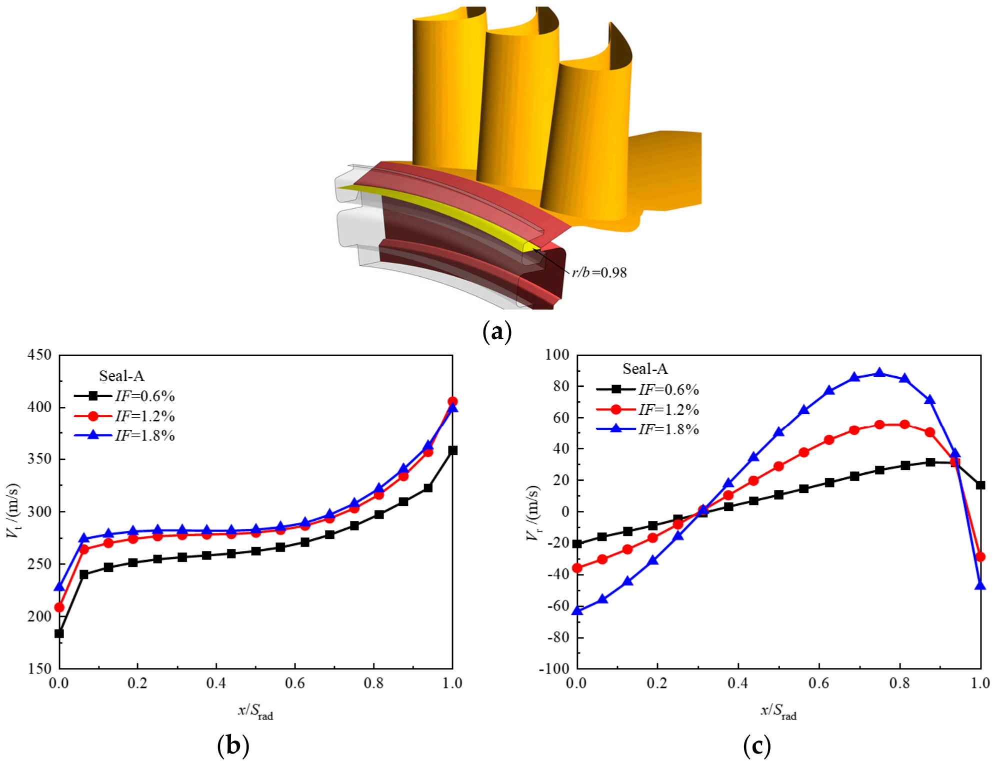

(**a**)

(**b**) (**c**)

Figure 15. Time-averaged tangential and radial velocity variations along the axial direction at the middle section of the sealing cavity: (**a**) position of the section in the middle of the sealing cavity; (**b**) time-averaged tangential velocity; and (**c**) time-averaged radial velocity.

In Figure 15b, it can be observed that the radial velocity distribution in the central section of the sealing cavity is relatively complex. The speed near the rotating disk is greater than zero, and the speed value near the stationary disk is less than zero, indicating that the cooling air flows radially out from the rotating disk side, and the gas intrudes near the static disk side. Comparing the radial velocity curves in Figure 15b, increasing the cooling air flow raises the maximum and minimum radial velocity magnitudes. The egress flow velocity near the rotating disk and the ingress velocity near the static disk both increase.

The larger the cooling air flow, the higher the maximum radial velocity, but its axial position is farther from the rotating disk. This is because a larger cooling air flow results in a higher axial velocity through the lower surface of the platform, so the airflow along the left side of the platform decreases, and more air flows radially outward, away from the rotating disk wall. The change in the radial outflow position also caused a change in the mainstream gas intruding along the outer surface of the platform, and a part of the mainstream gas intrudes along the left side of the platform. It can be seen from the curve that when $x/S_{\text{rad}} \approx 1$, the radial velocity drops rapidly and becomes negative, and this is more obvious for a larger cooling air flow rate.

The curves of the time-averaged sealing efficiency with the axial position in the middle plane of the sealing cavity are given in Figure 16. As the cooling air flow increases, the sealing efficiency continuously increases in most areas of the cavity. The average values of the sealing efficiency were 0.74, 0.88, and 0.93, from the highest to lowest cooling air flow ratios. Increasing the cooling air flow improves the sealing efficiency in the disk cavity. In the area near the rotating disk, the sealing efficiency decreases because the increased cooling air flow causes the radial outflow core area to move to the middle of the disk cavity, and the mainstream gas is forced to intrude at the platform surface.

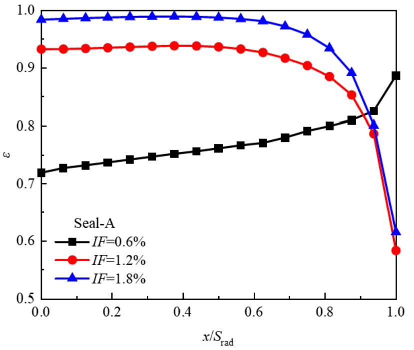

Figure 16. Time-averaged sealing efficiency variations along the axial direction at the middle section of the sealing cavity.

The time-averaged sealing efficiency contour distribution and the surface streamline at the ingress and egress sections in Seal-A are given in Figure 17. The time-averaged ingress sections are at the blade's leading edge, and the time-averaged egress sections are at the blade channel. The sealing structure in Figure 17 is Seal-A, and flow ratios of 0.6%, 1.2%, and 1.8% are selected.

In the egress section, the pressure outside the sealing clearance is lower than the pressure inside the disk cavity, and the cooling air flows into the main flow channel along the surface of the rotating disk because of the rotating pump effect. The cold air flow is relatively small when the flow ratio is 0.6%. The cooling air flows into the sealing cavity along the lower surface of the rim platform and then directly flows radially into the clearance outlet along the left side surface of the platform. The airflow forms two vortex structures, on the left side of the sealing cavity and at the rim platform's upper surface. With an increased cooling air ratio, the amount of cooling air flowing through the lower surface of the platform increases. The air no longer flows against the wall because of inertial effects but flows into the middle area of the sealing cavity first and then radially into the sealing outlet. On the one hand, an increase in cooling air flow strengthens the vortex structure in the sealing cavity, which occupies the entire left and lower area of the sealing cavity. On the other hand, the axial length of the return vortex at the sealing exit increases, and the vortex structure affects the area near the side surface of the platform.

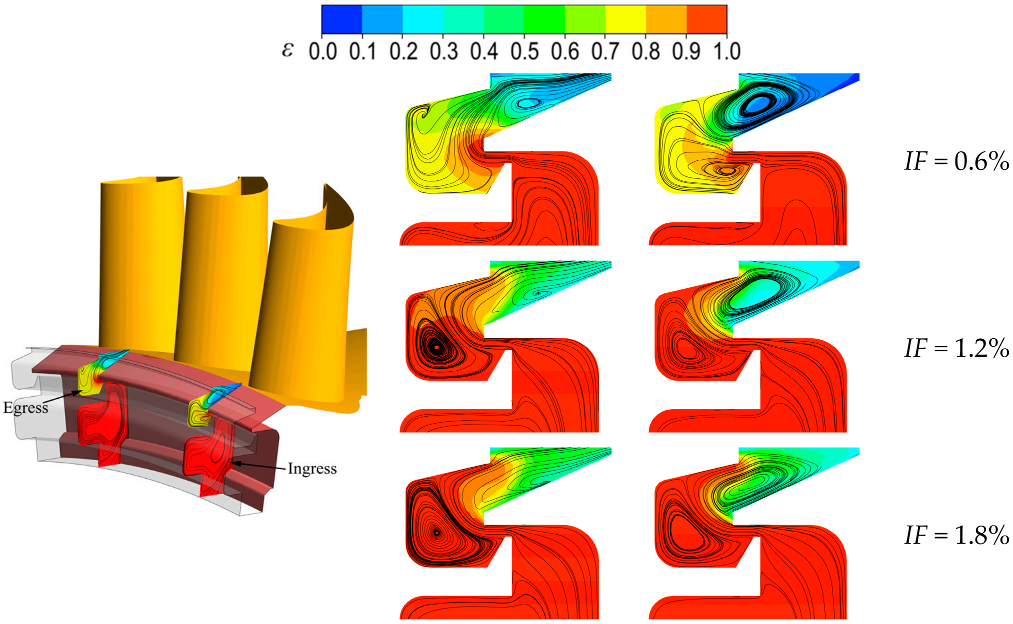

(**a**) (**b**) (**c**)

Figure 17. Time-averaged sealing efficiency contour distributions and the surface streamlines at the sections of ingress and egress in Seal-A: (**a**) position of the disk cavity sections; (**b**) egress section; (**c**) ingress section.

As can be seen from the sealing efficiency contours, the sealing efficiency of the seal's inner cavity is close to 100%, and the sealing cavity prevents further downward ingress of the mainstream gas. When the flow ratio is 0.6%, the cold air flows close to the left surface of the platform, so the sealing efficiency is high there. When the cold air flow rises, the vortex structure in the sealing cavity is enhanced, and a large amount of sealing cooling air is sucked, causing the sealing efficiency in the left and lower areas of the sealing cavity to increase. However, the reflux vortex at the sealing exit sucks in the mainstream gas and penetrates deeper into the sealing cavity, which causes gas ingress at the side surface of the platform, and the sealing efficiency decreases continuously there.

In the ingress section, the pressure outside the seal is higher than the pressure inside the disk cavity. The main flow gas invades the disk cavity, causing a change in its flow. The main flow gas intrudes along the upper surface of the platform and forms a return vortex in the sealing exit, where the vortex structure sucks up a large amount of the main flow gas and the mixed cooling air in the sealing cavity. The airflow in the lower area of the sealing cavity forms a reverse vortex, and the airflow contains part of the mainstream gas from the downward invasion and a large amount of the sealing cooling air. Two vortex structures occupy the entire sealing cavity and sealing outlet area.

From the sealing efficiency contours, the sealing efficiency of the inner cavity is still close to 100%. Gas ingress mainly occurs in the sealing cavity, and the two vortex structures keep the mainstream gas out of the sealing cavity. In the sealing exit area, the sealing efficiency is low in the area near the upper surface of the rim plate because the gas intrudes along the platform's upper surface. In the upper part of the sealing cavity, the cooling air is sucked into the reflux vortex, which increases the sealing efficiency there. In the sealing cavity, the reverse vortex sucks part of the downward-invading mainstream gas along the wall of the static disk. The sealing efficiency near the static disk is low. The sealing efficiency in the middle region of the sealing cavity is improved by the addition of a large amount of sealing cooling air. As the flow ratio increases, the cooling air entering the middle region of the sealing cavity along the lower surface of the platform increases. On the one hand, the reverse vortex in the sealing cavity is affected and occupies the lower-left area of the sealing cavity, and the sealing efficiency in this area improves rapidly. On the other hand, as the axial influence of the return vortex increases, the area near the platform surface affected by this vortex structure expands. However, the increased cooling air is also mixed into the return vortex at the sealing outlet, improving the overall sealing efficiency in this area.

The area-averaged sealing efficiencies at different disk cavity radii are given in Figure 18. The sealing efficiency of both the sealing cavity and the sealing outlet increases with the cooling air flow. Thus, increasing the sealing cold air volume is an effective way to improve the sealing performance of the disk cavity. The area-averaged sealing efficiency at the bottom of the sealing cavity ($0.96 < r/b < 0.975$) is less than that at the middle of the sealing cavity ($r/b \approx 0.975$). This is because the vortex structure in the sealing cavity sucks part of the mainstream gas into the bottom area along the surface of the static disk, decreasing the sealing efficiency there. The cooling air flows into the middle region of the sealing cavity along the lower surface of the rim platform, resulting in high sealing efficiency in this region. With an increase in the cooling air flow, the sealing efficiency in the middle region of the sealing cavity increases while also rapidly increasing in the lower region. The difference in the sealing efficiencies between the two regions decreases because more cooling air is sucked into the vortex structure inside the sealing cavity, thus rapidly increasing the local sealing efficiency. When the cooling air flow ratio increases from 0.6% to 1.8%, the sealing efficiency at the high radius increases by 30% on average.

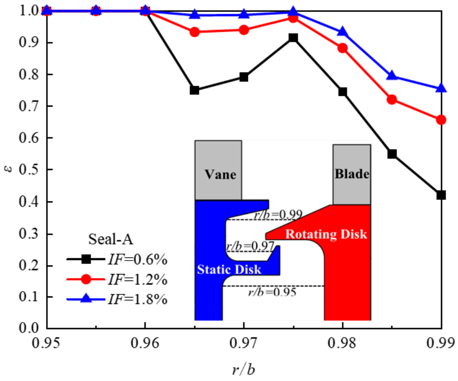

Figure 18. Sealing efficiency distribution along the disk cavity radial direction.

3.3. *Analysis of Sealing Structure Influence*

It is necessary to have a more detailed understanding of the disk cavity flow and pressure fields to characterize the influence of the deep cavity shape and the modified platform on the sealing performance. Therefore, Seal-A, Seal-B, and Seal-C are analyzed in this section. Figure 19 compares the circumferential C_p variations of the three sealing structures at $l1$ and $l2$.

From Figure 19a, the circumferential pressure variation curves of Seal-A, Seal-B, and Seal-C are the same at $l1$. The sealing structure changes do not significantly affect the pressure downstream of the vane trailing edge. As shown in Figure 19b, the circumferential pressure curves of the three sealing configurations at $l2$ are also consistent. Seal-B and Seal-C only affect the pressure near one of the blades, and the newly designed sealing structure may affect the egress flow, which in turn affects the circumferential pressure at the blade leading edge.

Comparing the time-averaged C_p and radial velocity contours of the three sealing structures at the same flow ratio in Figure 20, the distribution of the ingress and outflow areas at the sealing outlet of Seal-B does not change significantly compared to Seal-A. The deep sealing cavity has no significant impact on the ingress and outflow at the clearance outlet. For Seal-C, the area of negative radial velocity region increases, and the area of positive radial velocity region decreases slightly, indicating that the modified platform is not conducive to expanding the sealing outlet area but leads to more mainstream gas ingress into the disk cavity.

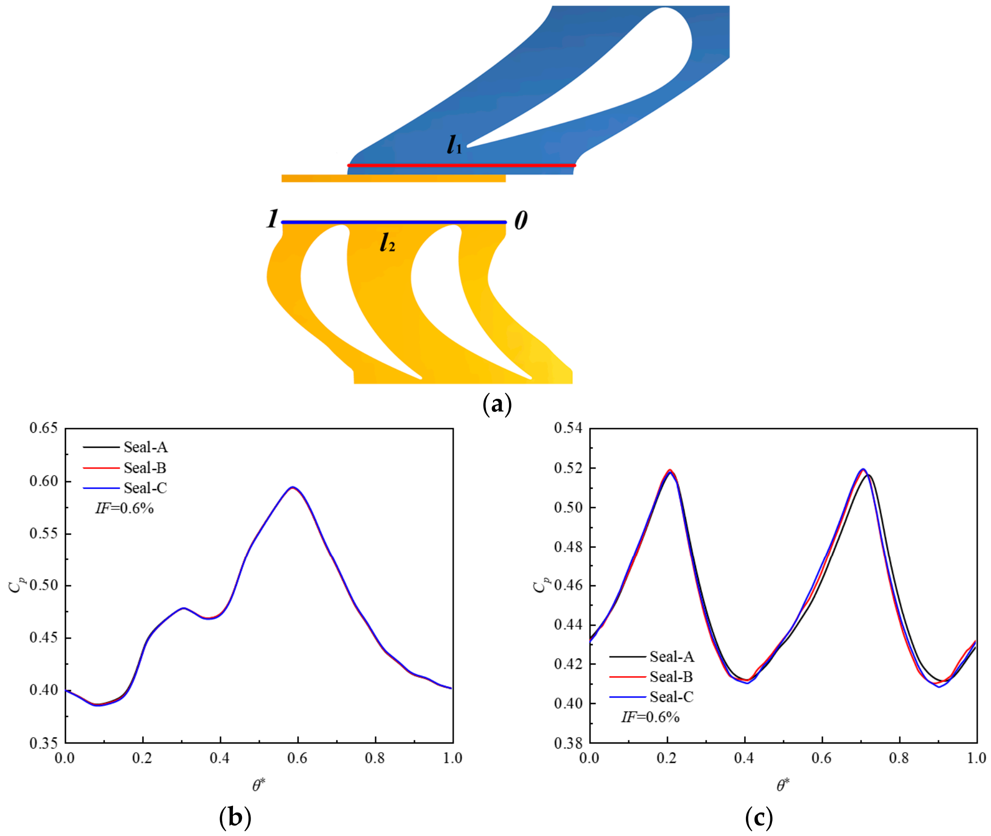

(**a**)

(**b**) (**c**)

Figure 19. Time-averaged static pressure coefficient distribution at *l*1 (downstream of the vane trailing edge) and *l*2 (upstream of the blade leading edge) for *IF* = 0.6%: (**a**) position of curves on the vane endwall and the blade endwall; (**b**) vane endwall; (**c**) blade endwall.

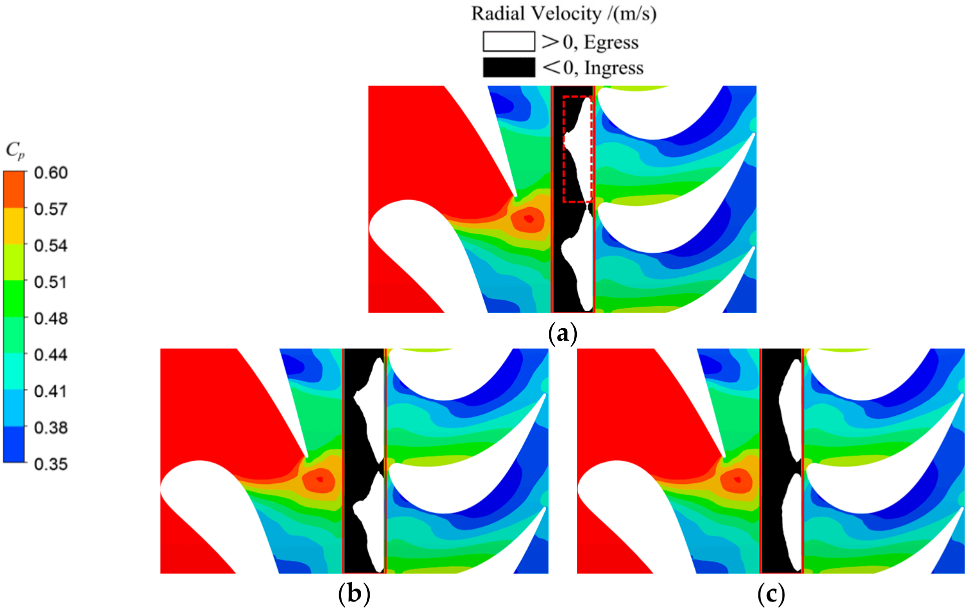

(**a**)

(**b**) (**c**)

Figure 20. Radial velocity contour distributions at the clearance outlet and static pressure coefficient distributions at the endwall for *IF* = 0.6%. (**a**) Seal-A; (**b**) Seal-B; (**c**) Seal-C.

The time-averaged tangential and radial velocity variations along the axial direction at the middle section of the sealing cavity (r/b = 0.98) are given in Figure 21. The three sealing structures have consistent tangential velocity variations in the middle section of the sealing cavity, and the tangential velocity increases as the axial position approaches the rotating disk from the static disk. When the tangential velocity curves of Seal-A and Seal-B in Figure 21a are compared, the deep cavity shape of the static disk causes a decrease in the tangential velocity at each axial position. In particular, the tangential velocity decrease is most obvious near the stationary disk surface of the deep cavity. The tangential velocities at axial positions $x/S_{\mathrm{ax}} > 0.5$ are higher than for the other two sealing structures because of the platform structure of Seal-C.

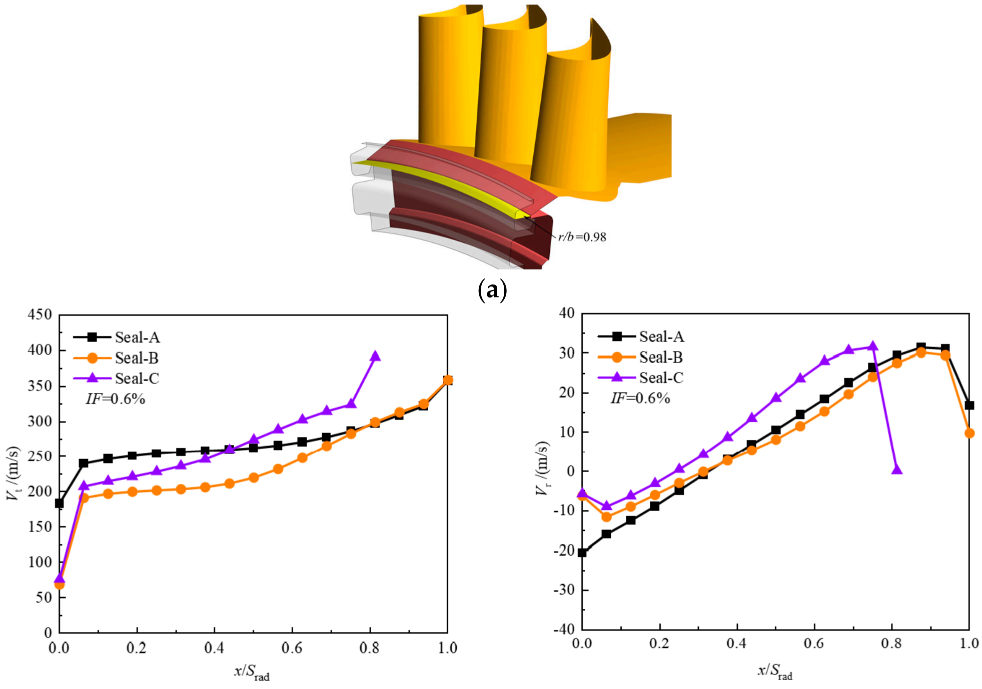

(**a**)

(**b**) (**c**)

Figure 21. Time-averaged tangential and radial velocity variations along the axial direction at the middle section of the sealing cavity for *IF* = 0.6%: (**a**) position of the section in the middle of the sealing cavity; (**b**) time-averaged tangential velocity; and (**c**) time-averaged radial velocity.

It can be observed in Figure 21b that the radial velocity near the rotating disk side is positive, and the velocity value near the static disk side is negative in the central section of the sealing cavity. In comparing the radial velocity curves of the three sealing structures, Seal-B's deep cavity shape decreases the cooling air flow's absolute radial velocity values near the rotating and static disks. This indicates that the radial outflow of the cooling airflow near the rotating disk and the ingress near the static disk both decrease in Seal-B. Because of the platform's influence, Seal-C has higher radial velocities than the other two seal structures at the same axial position. However, the radial velocity near the rotating disk and the middle of the sealing cavity is slightly lower than Seal-A, using the rotating disk surface as the reference point. The radial outflow in this region is weakened, the radial velocity near the static disk increases, and the ingress decreases.

The curves of the time-averaged sealing efficiency with the axial position in the middle plane of the sealing cavity are given in Figure 22. Seal-B and Seal-C have higher sealing efficiencies than Seal-A at different axial positions. The average face sealing efficiencies of Seal-A, Seal-B, and Seal-C in this cross-section are 0.74, 0.8, and 0.77, respectively. Compared with Seal-A, Seal-B increases the sealing efficiency by 8% because of its deep cavity shape in the static disk, and Seal-C increases the sealing efficiency by 4% after adding the platform shape.

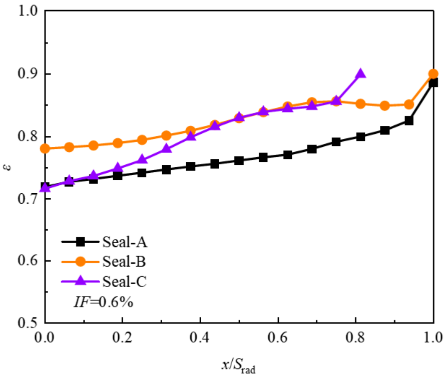

Figure 22. Time-averaged sealing efficiency variations along the axial direction at the middle section of the sealing cavity for *IF* = 0.6%.

Figures 23 and 24 detail the disk cavity's flow field for three sealing configurations at the flow ratios of 0.6% and 1.8%. Compared with Seal-A, the deep cavity shape in Seal-B only changes the flow field in the sealing cavity and has no significant effect on the return vortex at the sealing outlet. A new vortex structure is created in the lower concave cavity, both in the egress section and the ingress section, in addition to the reverse vortex in the left-side region of the sealing cavity. This is because part of the cooling air forms a return vortex in the lower concave cavity when it enters the sealing cavity along the lower surface of the platform, which consumes the cooling air. Therefore, the sealing efficiency in the concave cavity is close to 100%, as shown in the sealing efficiency contours. The deep cavity shape in the static disk and the cooling air significantly improve the sealing efficiency in the lower area of the sealing cavity compared to Seal-A.

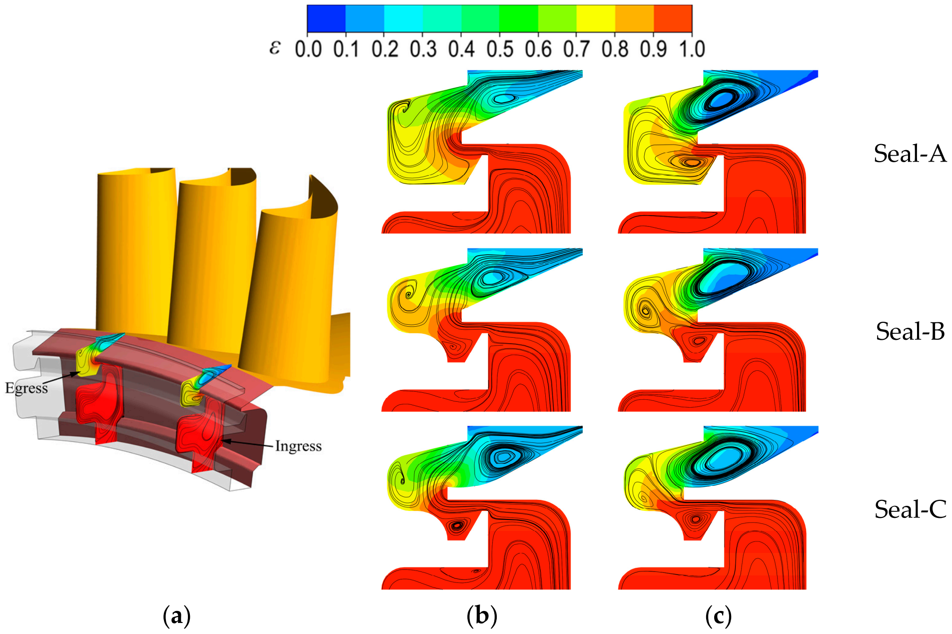

(**a**) (**b**) (**c**)

Figure 23. Time-averaged sealing efficiency contour distributions and surface streamlines at the sections of ingress and egress for *IF* = 0.6%: (**a**) position of the disk cavity sections; (**b**) egress section; (**c**) ingress section.

Based on Seal-B, Seal-C has a modified shape on the upper surface of the platform, and this new structure enlarges the area of the sealing exit. We know that the modified platform structure expands the influence of the return vortex in both the egress area and ingress areas at the sealed exit from the flow field structure. Combined with the sealing efficiency contours, this is not conducive to improving the sealing efficiency at the sealing exit. In addition, the platform structure transports the cooling air deeper into the sealing cavity. The return vortex in the lower recess of the sealing cavity still consumes the cooling air and keeps the sealing efficiency in this area high. However, it also reduces the reverse vortex on the left side of the sealing cavity and the expanding return vortex at the sealing outlet.

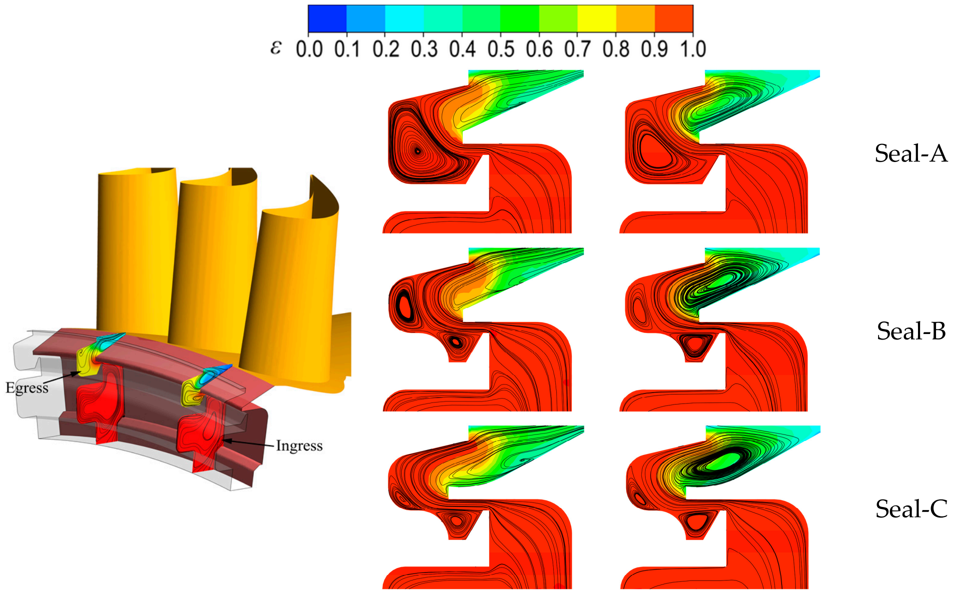

(**a**) (**b**) (**c**)

Figure 24. Time-averaged sealing efficiency contour distributions and surface streamlines at the sections of ingress and egress for *IF* = 1.8%: (**a**) position of the disk cavity sections; (**b**) egress section; (**c**) ingress section.

Figure 25 shows the sealing efficiency of the three sealing structures at different disk cavity radii. In the inner cavity ($r/b < 0.96$), the sealing efficiency of the three sealing structures is 100%. In the sealing cavity ($0.96 < r/b < 0.975$), Seal-C has the best sealing performance, and Seal-A has the worst performance. Therefore, the deep cavity shape in the static disk effectively improves the sealing cavity efficiency. In the sealing exit region ($r/b \geq 0.985$), Seal-C has the lowest seal efficiency, and Seal-B has the highest. Thus, using the modified platform structure is not conducive to improving the sealing efficiency at the sealing exit but enhances the sealing efficiency in the sealing cavity. In general, compared with Seal-A, the sealing efficiency of Seal-B and Seal-C is increased by 13.5% and 10%, respectively, at *IF* = 0.6%.

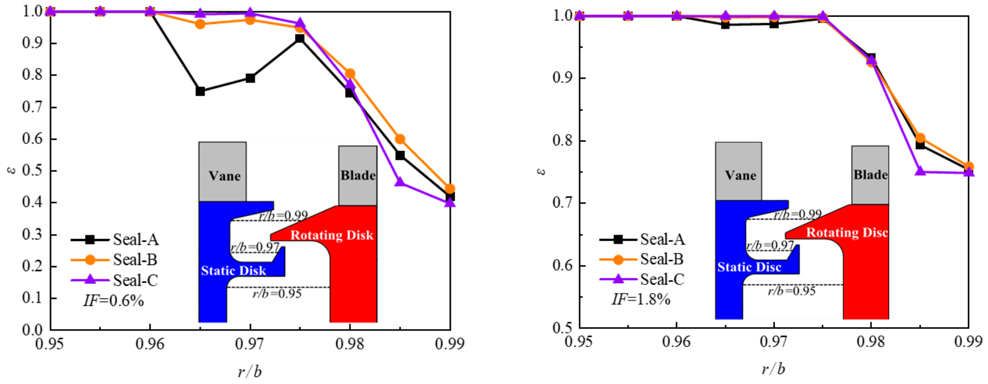

(**a**) (**b**)

Figure 25. Sealing efficiency distribution along the radial direction in the disk cavity: (**a**) *IF* = 0.6%; and (**b**) *IF* = 1.8%.

4. Conclusions

This paper studies the sealing characteristics of different sealing structures in a high-pressure turbine under actual conditions by solving the three-dimensional URANS equations and SST k-ω turbulence model. The unsteady flow characteristics at the sealing clearance, the influence of different sealing structures, and cooling air flow rates on the sealing efficiency, and the flow field in the disk cavity are obtained, which provides a reference for further optimization of the sealing structure. The main conclusions are as follows.

(1) The interference of the vane and blade dominates the effect on the sealing outlet pressure, which has a significant impact on the sealing performance. The gas ingress and egress flow in the transient calculation are more dramatic than in the steady-state calculation. The turbine studied in this paper is a transonic turbine. The sealing clearance is not only affected by the high-pressure area at the trailing edge of the vane and the blade leading edge but also by the local high-pressure area caused by the shock wave at the vane suction surface, which intensifies the gas ingress in the sealing clearance area.

(2) Increased cooling air flow increases the tangential velocity in the sealing cavity and the radial velocity near the rotating/static disk sides. The reverse vortex in the sealing cavity is enhanced, and the sealing efficiency of the disk cavity is continuously improved. When the cooling air flow ratio increases from 0.6% to 1.8%, the sealing efficiency at the high radius increases by 30%. Increasing the cooling air flow also enhances the egress flow, and the static pressure values downstream of the vane trailing edge and upstream of the blade leading edge are thus increased, and the circumferential pressure difference is reduced.

(3) Seal-A has inherently better sealing performance. Even in the gas ingress area, the reverse vortex in the sealing cavity and the return vortex in the sealing exit retain the gas outside the sealing cavity, ensuring a high sealing efficiency of the inner cavity. Seal-B and Seal-C do not influence the pressure distribution downstream of the vane trailing edge but only affect the pressure distribution upstream of the blade leading edge. The deep cavity shape in Seal-B only changes the flow field in the sealing cavity. A return vortex is created when the cooling air flows through the lower part of the sealing cavity, which intensifies the gas ingress. The platform structure in Seal-C increases the ingress area at the sealing exit and intensifies the gas ingress in this area, but the modified platform's structure helps improve the sealing efficiency at the low radius of the sealing cavity. In general, compared with Seal-A, the sealing efficiency of Seal-B and Seal-C is increased by 13.5% and 10%, respectively, at $IF = 0.6\%$.

Author Contributions: Conceptualization, Writing—Original Draft, Q.Z.; Methodology, Software, Q.W.; Writing—Review and Editing, Data Curation, Validation, X.T.; Visualization, Supervision, J.Z. All authors have read and agreed to the published version of the manuscript.

Funding: The authors gratefully acknowledge the financial support for this project from the National Science and Technology Major Project(2017-III-0001-0025), Nanjing University of Aeronautics and Astronautics under Grant.

Institutional Review Board Statement: Not applicable.

Informed Consent Statement: Not applicable.

Data Availability Statement: Not applicable.

Conflicts of Interest: The authors declare no conflict of interest.

Nomenclature

b	rim seal radius (mm)
c	tracer gas concentration
S_{ax}	sealing axial clearance (mm)
S_{rad}	sealing radial clearance (mm)

Re_w	axial Reynolds number ($\rho v b/\mu$)
P_s	static pressure (Pa)
v	annulus axial velocity (m/s)
T	time for the blade to pass through a vane channel (s)
$P_{t,in}$	total pressure at the mainstream annulus inlet (Pa)
f_blade	frequency at which the blade rotates through a vane channel (Hz)
IF	ratio of the cooling airflow rate to the mainstream flow rate
Re_Ω	rotational Reynolds number ($\rho \omega b^2/\mu$)
S	axial clearance between rotor and stator (mm)
C_p	pressure coefficient ($P_\mathrm{s}/P_{t,in}$)
Greek symbols	
ρ	density (kg/m^3)
μ	dynamic viscosity (kg/(m·s))
θ	circumferential angle (°)
ω	rotational angular velocity (rad/s)
θ^*	dimensionless circumferential angle
ε	sealing efficiency
Subscripts	
ax	axial direction
rad	radial direction
0	initial position
1	final position
∞	annulus inlet
coolant	cooling air inlet

References

1. Fiore, M.; Gourdain, N.; Boussuge, J.-F.; Lippinois, E. Delineating loss sources within a linear cascade with upstream cavity and purge flow. *ASME J. Turbomach.* **2019**, *141*, 091008. [CrossRef]
2. Lian, Z.Y.; Du, Q.; Liu, G.; Wang, R.N.; Xie, L. Numerical investigation on unsteady characteristics in different rim seal geometries: Part B. In Proceedings of the ASME Turbo Expo 2020: Turbomachinery Technical Conference and Exposition, Virtual, 21–25 September 2020.
3. Laskowski, G.M.; Bunker, R.S.; Bailey, J.C.; Ledezma, G.; Kapetanovic, S.; Itzel, G.M.; Sullivan, M.A.; Farrell, T.R. An investigation of turbine wheelspace cooling flow interactions with a transonic hot gas path—Part II: CFD simulations. *ASME J. Turbomach.* **2011**, *133*, 041020. [CrossRef]
4. Li, Z.; Yang, F.; Wang, Z.X. Numerical investigation of the blockage effect caused by rim seal flow. *Proc. Inst. Mech. Eng. Part G* **2020**, *234*, 1433–1445. [CrossRef]
5. Owen, J.M.; Tang, H.; Lock, G.D. Model of effect of hot gas ingress on temperatures of turbine disks. *ASME J. Eng. Gas Turbines Power* **2019**, *141*, 012501. [CrossRef]
6. Balasubramanian, J.; Junnarkar, N.; Zhou, D.W.; Roy, R.P.; Kim, Y.W.; Moon, H.K. Experiments on aft-disk cavity ingestion in a model 1.5-stage axial-flow turbine. In Proceedings of the ASME 2011 Turbo Expo: Turbine Technical Conference and Exposition, Vancouver, BC, Canada, 6–10 June 2011.
7. Bunker, R.S. Gas turbine heat transfer: Ten remaining hot gas path challenges. *ASME J. Turbomach.* **2007**, *129*, 193–201. [CrossRef]
8. Scobie, J.A.; Sangan, C.M.; Owen, J.M.; Lock, G.D. Review of ingress in gas turbines. *ASME J. Eng. Gas Turbines Power* **2016**, *138*, 120801. [CrossRef]
9. Koff, B.L. Gas turbine technology evolution: A designer's perspective. *J. Propuls. Power* **2004**, *20*, 577–595. [CrossRef]
10. He, Z.; Zhou, J.; Yang, C.; Li, B.; Qian, J. Unsteady numerical investigation on gas ingestion into the rotor-stator disk cavities of a 1.5-stage turbine. *Aeronaut. J.* **2022**, *126*, 1718–1735. [CrossRef]
11. Phadke, U.P.; Owen, J.M. An investigation of ingress for an air-cooled shrouded rotating disk system with radial-clearance seals. *ASME J. Eng. Gas Turbines Power* **1983**, *105*, 178–182. [CrossRef]
12. Phadke, U.P.; Owen, J.M. Aerodynamic aspects of the sealing of gas-turbine rotor-stator systems: Part 1: The behavior of simple shrouded rotating-disk systems in a quiescent environment. *Int. J. Heat Fluid Flow* **1988**, *9*, 98–105. [CrossRef]
13. Phadke, U.P.; Owen, J.M. Aerodynamic aspects of the sealing of gas-turbine rotor-stator systems: Part 2: The performance of simple seals in a quasi-axisymmetric external flow. *Int. J. Heat Fluid Flow* **1988**, *9*, 106–112. [CrossRef]
14. Phadke, U.P.; Owen, J.M. Aerodynamic aspects of the sealing of gas-turbine rotor-stator systems: Part 3: The effect of nonaxisymmetric external flow on seal performance. *Int. J. Heat Fluid Flow* **1988**, *9*, 113–117. [CrossRef]
15. Owen, J.M. Prediction of ingestion through turbine rim seals-part I: Rotationally induced ingress. *ASME J. Turbomach.* **2011**, *133*, 031005. [CrossRef]

16. Owen, J.M. Prediction of ingestion through turbine rim seals-part II: Externally induced and combined ingress. *ASME J. Turbomach.* **2011**, *133*, 031006. [CrossRef]
17. Sangan, C.M.; Pountney, O.J.; Zhou, K.Y.; Wilson, M.; Owen, J.M.; Lock, G.D. Experimental measurements of ingestion through turbine rim seals-part I: Externally-induced ingress. *ASME J. Turbomach.* **2013**, *135*, 021012. [CrossRef]
18. Sangan, C.M.; Pountney, O.J.; Zhou, K.Y.; Owen, J.M.; Wilson, M.; Lock, G.D. Experimental measurements of ingestion through turbine rim seals-part II: Rotationally-induced ingress. *ASME J. Turbomach.* **2013**, *135*, 021013. [CrossRef]
19. Sangan, C.M.; Pountney, O.J.; Scobie, J.A.; Wilson, M.; Owen, J.M.; Lock, G.D. Experimental measurements of ingestion through turbine rim seals-part III: Single and double seals. *ASME J. Turbomach.* **2013**, *135*, 051011. [CrossRef]
20. Sangan, C.M.; Scobie, J.A.; Owen, J.M.; Lock, G.D.; Tham, K.M.; Laurello, V.P. Performance of a finned turbine rim seal. *ASME J. Turbomach.* **2014**, *136*, 111008. [CrossRef]
21. Jia, X.Y.; Zhang, H.; Jiang, Y.T. Performance of radial-axial clearance rim seal in realistic working conditions. *Aerosp. Sci. Technol.* **2018**, *77*, 373–387. [CrossRef]
22. Savov, S.S.; Atkins, N.R.; Uchida, S. A comparison of single and double lip rim seal geometries. *ASME J. Eng. Gas Turbines Power* **2017**, *139*, 112601. [CrossRef]
23. Popovic, I.; Hodson, H.P. Improving turbine stage efficiency and sealing effectiveness through modifications of the rim seal geometry. *ASME J. Turbomach.* **2013**, *135*, 061016. [CrossRef]
24. Moon, M.A.; Lee, C.S.; Kim, K.Y. Effect of a rib on rim seal performance. *Int. Commun. Heat Mass Transf.* **2014**, *59*, 130–135. [CrossRef]
25. DA Soghe, R.; Bianchini, C.; Micio, M. Effect of rim seal configuration on gas turbine cavity sealing in both design and off-design conditions. In Proceedings of the ASME Turbo Expo 2018: Turbomachinery Technical Conference and Exposition, Oslo, Norway, 11–15 June 2018.
26. Scobie, J.A.; Teuber, R.; Li, Y.S.; Sangan, C.M.; Wilson, M.; Lock, G.D. Design of an improved turbine rim seal. *ASME J. Eng. Gas Turbines Power* **2016**, *138*, 022503. [CrossRef]
27. Schuler, P.; Kurz, W.; Dullenkopf, K.; Bauer, H.-J. The influence of different rim seal geometries on hot-gas ingestion and total pressure loss in a low-pressure turbine. In Proceedings of the ASME Turbo Expo 2010: Power for Land, Sea, and Air, Glasgow, UK, 14–18 June 2010; pp. 1123–1134.
28. Schuler, P.; Dullenkopf, K.; Bauer, H.-J. Investigation of the influence of different rim seal geometries in a low-pressure turbine. In Proceedings of the ASME 2011 Turbo Expo: Turbine Technical Conference and Exposition, Vancouver, BC, Canada, 6–10 June 2011; pp. 715–729.
29. Li, J.; Gao, Q.; Li, Z.G.; Feng, Z.P. Numerical investigations on the sealing effectiveness of turbine honeycomb radial rim seal. *ASME J. Eng. Gas Turbines Power* **2016**, *138*, 102601. [CrossRef]
30. Erickson, R.D.; Simon, T.W.; Zhang, L.Z.; Moon, H.-K. Experimental investigation of disc cavity leakage flow and hub endwall contouring in a linear rotor cascade. In Proceedings of the ASME 2011 Turbo Expo: Turbine Technical Conference and Exposition, Vancouver, BC, Canada, 6–10 June 2011; pp. 1769–1780.
31. Zhang, Z.Q.; Zhang, Y.J.; Dong, X.; Qu, X.; Lu, X.G.; Zhang, Y.F. Flow mechanism between purge flow and mainstream in different turbine rim seal configurations. *Chin. J. Aeronaut.* **2020**, *33*, 2162–2175. [CrossRef]
32. Schuepbach, P.; Abhari, R.S.; Rose, M.G.; Gier, J. Sensitivity of turbine efficiency and flow structures to varying purge flow. *J. Propuls. Power* **2010**, *26*, 46–56. [CrossRef]
33. Da Soghe, R.; Bianchini, C.; Mazzei, L.; Bonini, A.; Innocenti, L.; Benedetto, D.D.; Orsini, L. On the extrapolation of rim sealing performance from test bench to real engine: A numerical survey. *ASME J. Eng. Gas Turbines Power* **2022**, *144*, 041001. [CrossRef]
34. Scobie, J.A.; Hualca, F.P.; Sangan, C.M.; Lock, G.D. Egress interaction through turbine rim seals. *ASME J. Eng. Gas Turbines Power* **2018**, *140*, 072504. [CrossRef]
35. Li, X.J.; Zhang, J.Z.; Tan, X.M.; Wang, Y. Enhancing forced-convection heat transfer of a channel surface with piezo-fans. *Int J Mech Sci.* **2022**, *227*, 107437. [CrossRef]
36. Choi, S.; Bang, M.; Choi, S.M.; Cho, M.H.; Moon, H.K.; Cho, H.H. Unsteady hot gas ingestion through the double rim-seals of an axial gas turbine. *Int. J. Mech. Sci.* **2021**, *207*, 106664. [CrossRef]
37. Cheng, S.X.; Li, Z.G.; Li, J. Effects of endwall profiling near the blade leading edge on the sealing effectiveness of turbine rim seal. *Proc. Inst. Mech. Eng. Part A* **2019**, *233*, 821–833.
38. Cheng, S.X.; Li, Z.G.; Li, J. Investigations on the sealing effectiveness and unsteady flow field of 1.5-stage turbine rim seal. *ASME J. Eng. Gas Turbines Power* **2019**, *141*, 081003. [CrossRef]
39. Jia, X.Y.; He, L.D.; Zhang, H. Effect of turbine rotor disc vibration on hot gas ingestion and rotor-stator cavity flow. *Aerosp. Sci. Technol.* **2020**, *98*, 105719. [CrossRef]
40. Wang, X.J.; Liao, G.L.; Zhang, F.; Li, J. Numerical investigation on the steady and unsteady flow characteristics of rim seal for the first stage in gas turbine. *Appl. Therm. Eng.* **2016**, *99*, 11–22. [CrossRef]